Flat band induced quantum criticality in a nonsuperconducting iron pnictide

Zhonghao Liu,[1,2,*] Huican Mao,[3] Yasuyuki Nakajima,[4] Johnpierre Paglione,[5,6] Zhiping Yin,[3,7,†] and Sergey Borisenko[8,‡]

[1]*School of Physical Science and Technology, Ningbo University, Ningbo 315211, China*
[2]*Institute of High-Pressure Physics, Ningbo University, Ningbo 315211, China*
[3]*Department of Physics and Center for Advanced Quantum Studies, Beijing Normal University, Beijing 100875, China*
[4]*Department of Physics, University of Central Florida, Orlando, Florida 32816, USA*
[5]*Maryland Quantum Materials Center and Department of Physics, University of Maryland, College Park, Maryland 20742, USA*
[6]*Canadian Institute for Advanced Research, Toronto, Ontario M5G 1Z8, Canada*
[7]*Key Laboratory of Multiscale Spin Physics, Ministry of Education, Beijing Normal University, Beijing 100875, China*
[8]*IFW-Dresden, Helmholtzstrate 20, Dresden 01171, Germany*

(Received 2 November 2023; revised 17 December 2023; accepted 17 January 2024; published 2 February 2024)

Flat electronic bands at the Fermi energy (E_F) can induce interaction-driven instabilities and further result in the emergence of a plethora of new quantum phases such as Mott insulators, ferromagnetism, fractional quantum Hall states even at high temperatures, and superconductivity. Except for flat bands in f-electron systems and special geometric lattices, however, the materials with quantum criticality induced by flat bands just at E_F remain elusive. Here, by using angle-resolved photoemission spectroscopy and band structure calculations, we present a comprehensive study of the low-energy electronic structure of a nonsuperconducting iron pnictide, $Ba(Fe_{1/3}Co_{1/3}Ni_{1/3})_2As_2$, which is a quantum-critical $3d$ transition metal alloy. We demonstrate the existence of a dispersionless flat band of t_{2g} orbitals just at E_F which is responsible for quantum critical behaviors. Our findings will promote studies of emergent physics induced by flat bands, such as non-Fermi-liquid behaviors and quantum critical phenomena in $3d$ transition metals.

DOI: 10.1103/PhysRevB.109.075103

I. INTRODUCTION

A flat electronic band is dispersionless over a finite range of momentum usually with superheavy, localized electrons, extremely singular density of states, and strongly correlated states. Materials with flat bands in the vicinity of the Fermi energy (E_F) are a promising platform to explore abundant quantum phases such as ferromagnetism [1], Mott insulators [2], fractional quantum Hall states even at high temperatures [3–5], and superconductivity [6]. For instance, flat f-electron band induced magnetic order, magnetically mediated superconductivity, and non-Fermi-liquid ground state in heavy fermions have been intensively investigated in condensed-matter physics [7]. Recent studies have found that flat bands can be constructed in special geometric lattices, like kagome [8–16] or morié lattices [2,6]. However, flat bands in kagome materials are usually not just at E_F and are difficult to tune properly to induce novel quantum phases. Large-scale and stable artificial materials with magical angles in morié lattices are also hard to achieve. Except for flat bands in kagome-lattice $3d$ transition metals due to quantum destructive interference, $3d$-electron flat bands have been long sought theoretically and experimentally. Therefore, finding a real $3d$ material with quantum critical behaviors induced by a flat band just right at E_F is essential to exploit flat band induced emergent physics, as well as understand the underlying physics for quantum criticality.

Iron pnictide superconductors such as $A(Fe_{1-x}Co_x)_2As_2$ (A = Ba, Sr, and Ca) exhibit strong doping- and orbital-dependent physics [17–31]. In the superconducting regime, the low-lying energy bands in the vicinity of E_F are dominated by the t_{2g} orbitals, which are more correlated than the e_g ones. The d_{xy} orbital especially is the most correlated of all [17–23]. Along with the increased filling of the electronic $3d$ shell, the chemical potential is shifted up and the strength of the electronic correlation is almost equal among the t_{2g} orbitals upon the half substituted AFeCoAs$_2$ [19,20]. In fully doped ACo_2As_2 [22–25,29], the e_g orbitals fall on E_F and begin to play a dominant role in the system. Recent investigations indicate that a flat band of the e_g orbitals near E_F, especially d_{x2-y2}, is responsible for magnetic instabilities resulting in doping- and magnetic-field-tuned quantum critical phenomena [24–27]. $Ba(Fe_{1/3}Co_{1/3}Ni_{1/3})_2As_2$ is isoelectronic to $BaCo_2As_2$ due to electron compensation by the equivalent of Fe and Ni substitutions. As a nonsuperconducting material, its non-Fermi-liquid behaviors and quantum critical phenomena have been observed by measuring anomalous temperature-dependent transport properties [28].

In this work, we demonstrate a dispersionless flat band of t_{2g} orbitals at E_F and a linearly dispersive band of d_{xy} orbitals around the Brillouin zone (BZ) corners in $Ba(Fe_{1/3}Co_{1/3}Ni_{1/3})_2As_2$ employing angle-resolved photoemission spectroscopy (ARPES) and band structure calculations. The flat band just at E_F is responsible for quantum critical behaviors, and an anomalous scattering rate in the

*liuzhonghao@nbu.edu.cn
†yinzhiping@bnu.edu.cn
‡s.borisenko@ifw-dresden.de

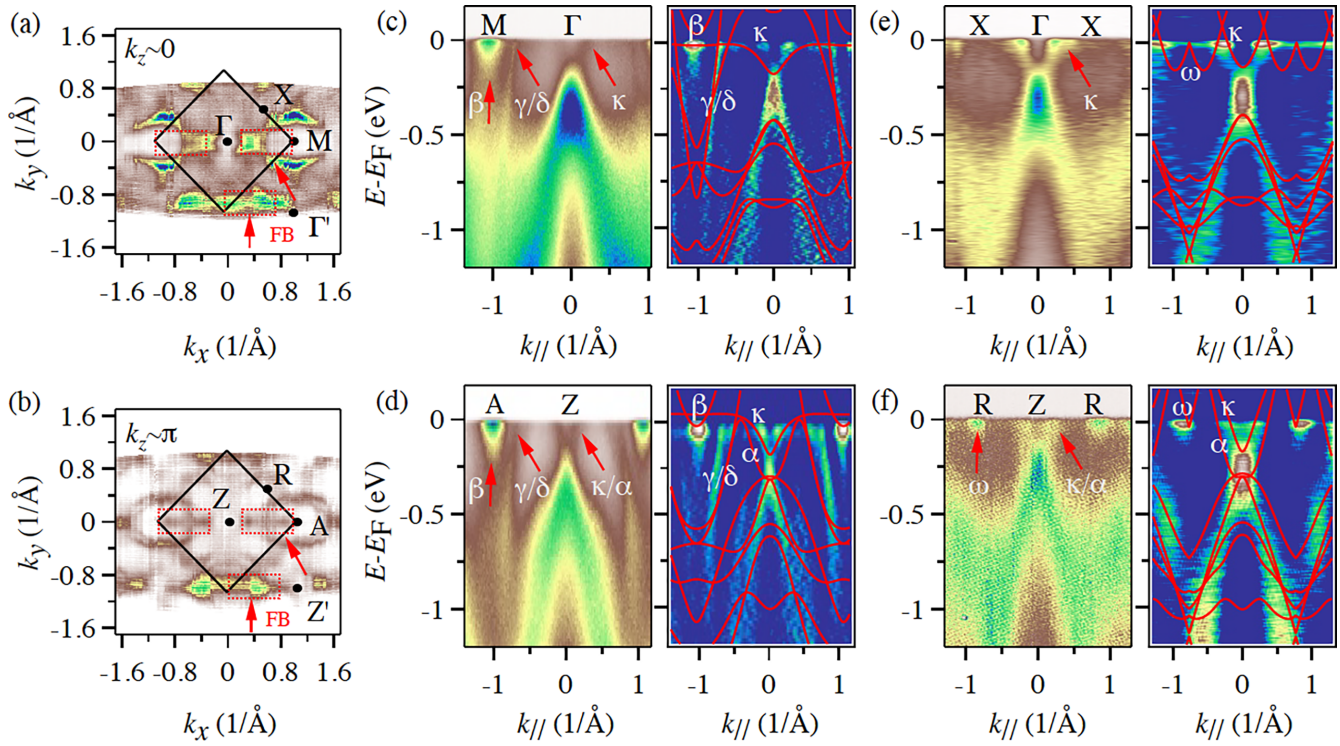

FIG. 1. (a) and (b) Integrated intensity plots at $E_F \pm 10$ meV taken on the $k_z \sim 0$ (Γ-X-M) and $k_z \sim \pi$ (Z-R-A) plane, respectively. The black solid lines indicate the two-dimensional BZ projected on the (001) surface. The red frames indicated by the arrow lines show shadowy FSs formed by the flat band. (c) and (d) Intensity plots and corresponding second derivative plots along the Γ-M and Z-A directions, respectively. (e) and (f) The same as (c) and (d), but along the Γ-X and Z-R directions, respectively. The bands near E_F are indicated by the red arrow lines on the intensity plots and are marked on the corresponding second derivative plots. The red solid lines on the corresponding second derivative plots are DFT-calculated bands renormalized by a factor of 1.4.

linear band up to 100 meV below E_F shows non-Fermi-liquid behaviors. Our findings provide insights into the underlying physics for quantum criticality in 3d transition metals.

II. METHODS

High-quality single crystals of $Ba(Fe_{1/3}Co_{1/3}Ni_{1/3})_2As_2$ were synthesized by the self-flux method with the molar ratios of Ba:FeAs:CoAs:NiAs = 3:4:4:4 as described elsewhere [28]. ARPES measurements were performed at a 1^3-ARPES end station at BESSY II within a wide range of photon energies. The energy and momentum resolutions were set to better than about 15 meV and 0.02 $Å^{-1}$, respectively. Samples with a size smaller than 1×1 mm^2 were cleaved *in situ*, yielding flat mirror-like (001) surfaces. Temperature was set at 30 K for the mapping of the Fermi surfaces (FSs), and set at 1 K for the measuring of feature bands. The pressure was maintained less than 5×10^{-11} Torr. The electronic structures were calculated with density functional theory (DFT) using the linearized augmented plane wave method as implemented in WIEN2K [32] combined with the Perdew-Burke-Ernzerhof form of the general gradient approximation to the exchange-correlation functional [33]. The experimental crystal structures (space group I4/mmm, No. 139) of $BaCo_2As_2$ with lattice constants $a = 3.9537$ Å, $c = 12.6524$ Å, and $z_{As} = 1.278$ Å [34] and $Ba(Fe_{1/3}Co_{1/3}Ni_{1/3})_2As_2$ with lattice constants $a = 3.9920$ Å, $c = 12.6191$ Å, and $z_{As} = 1.282$ Å [28] were used in the calculations.

III. RESULTS AND DISCUSSIONS

Figures 1(a) and 1(b) show the measured FSs of $Ba(Fe_{1/3}Co_{1/3}Ni_{1/3})_2As_2$ at 30 K on the $k_z \sim 0$ (Γ-X-M) and the $k_z \sim \pi$ (Z-R-A) plane, taken by the photon energies of 82 eV and 100 eV, respectively. To identify which FSs are represented by intensity spots on the maps, we recorded the energy-momentum distributions of the photocurrents along the Γ-M (Z-A) and Γ-X (Z-R) directions, respectively, as shown in Figs. 1(c)–1(f). The red solid lines appended on second derivative plots are DFT calculated bands, renormalized by a factor of ~1.4 to match the main dispersive features. This value implies weak electron correlation effects, as was the case in ACo_2As_2 [22,29]. These intensity plots and the calculated bands clearly show that electron pockets dominate FSs. The γ/δ bands form big electron pockets around the BZ corners (the M and A points), as the typical bands at the BZ corner in heavily electron-doped iron pnictides [20–25]. A hot spot (β) at the BZ corners is formed by an electronlike band bottom entangled with the κ band extending from the BZ center. The κ band is very flat along the Γ-M and Z-A directions predicted by the calculation, which corresponds to experimentally measured shadowy FSs on the integrated intensity plots as indicated by the red frames in Figs. 1(a) and 1(b). Though this flat band along Γ-M is closer to E_F than that along Z-A in the calculation, the corresponding shadowy FSs formed by the flat band look more distinct along Z-A due to the matrix element effects and Fermi energy cutoff related to

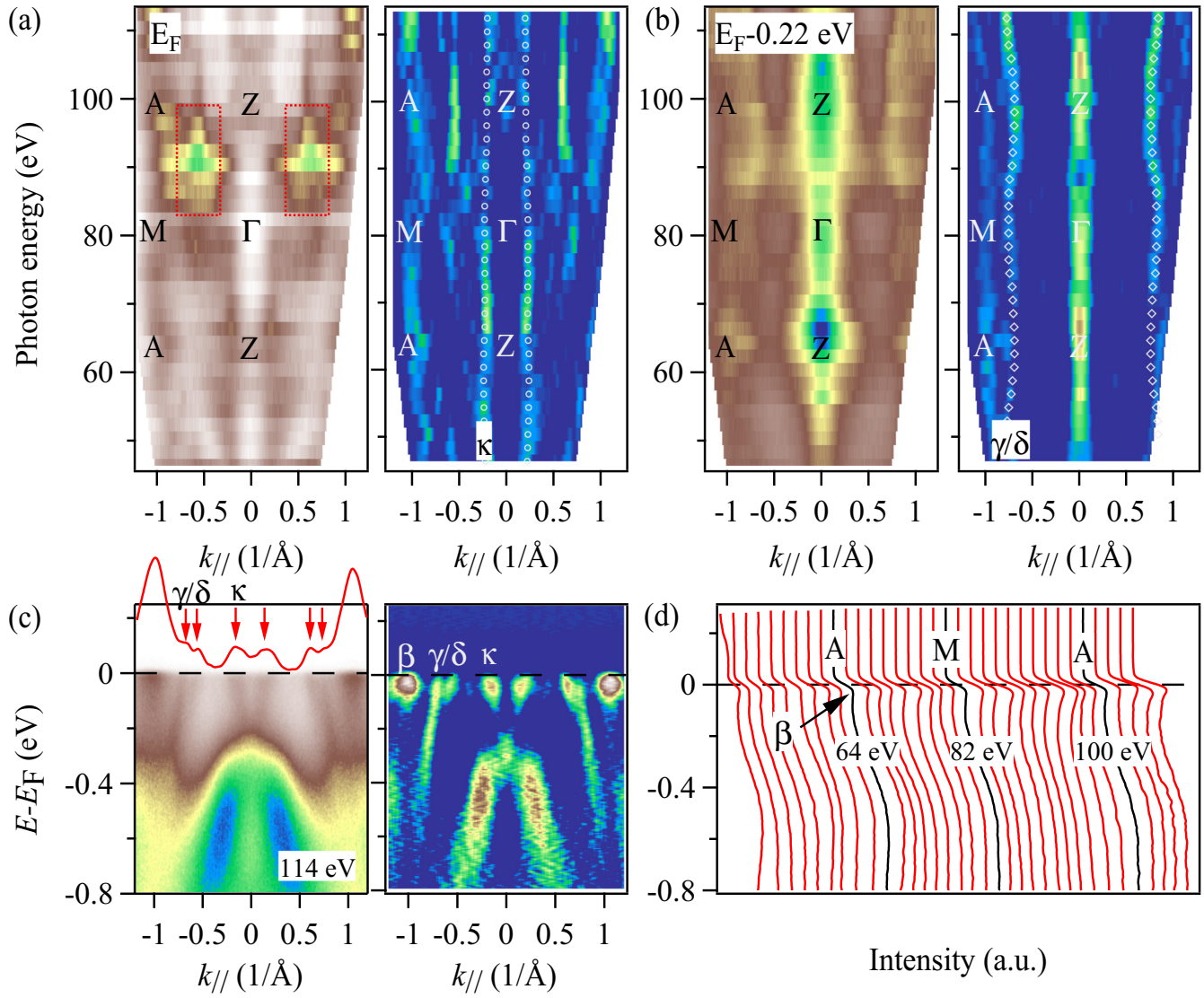

FIG. 2. (a) and (b) Integrated intensity plots (±10 meV) and corresponding second derivative plots on the $k_{//}$-k_z plane taken at E_F and E_F-0.22 eV, respectively. Photon energies used for the k_z dispersion measurement were from 46 to 114 eV. High-symmetry points and the band names are indicated. The shadows from the flat bands indicated by the red frames in the integrated intensity plots are enhanced from around 84 to 98 eV due to the matrix element effects. (c) Intensity plot and corresponding second derivative plot along the Γ-M direction taken by photon energy of 114 eV ($k_z \sim \pi/2$). The appended red solid curve is MDC at E_F. The peaks indicated by the red arrows are the band-crossing point at E_F. (d) EDCs along the A-M-A direction.

k_z dispersions. Additionally, the calculation indicates the γ/δ bands far away from the flat part of κ. We therefore study this flat band not only around the high-symmetry planes but also on the other k_z planes, as discussed later.

Along the Γ-X direction [Fig. 1(e)], the ω band around the X point escapes from experimental observation due to matrix element effects and just leaves weak intensity at E_F as shown on the integrated FS plot of Fig. 1(a). Compared with the measured bands, the calculated ω band needs to be further shifted up and the calculated β band needs to be further shifted down after global renormalization, indicating much more complicated electronic correlation effects and interband coupling at E_F. The measured band structures on the $k_z \sim \pi$ (Z-R-A) plane are similar to those on the $k_z \sim 0$ (Γ-X-M) plane, except that the α band appears at the Z point and the ω band bottom appears at the R point due to k_z dispersions. We note that the α band with the strong k_z dispersion gets entangled with the κ band along with various photon polarizations and energies.

To investigate k_z dispersions in detail, we carried out measurements using photon energies ($h\nu$) from 46 to 114 eV, which covers more than 1.5 BZs along k_z. With an empirical value of inner potential of 11 eV and $c' = c/2 = 6.3096$ Å (due to bilayer FeAs), we found that $h\nu = 48$ and 82 eV are close to the Γ point, and 64 and 100 eV are close to the Z point, according to the free electron final-state model [31]. Figures 2(a) and 2(b) show the intensity as a function of photon energy and $k_{//}$ oriented along the Γ-M (Z-A) direction, taken at E_F and $E_F-0.22$ eV, respectively. The band-crossing points at E_F are indicated by the red arrow lines on momentum

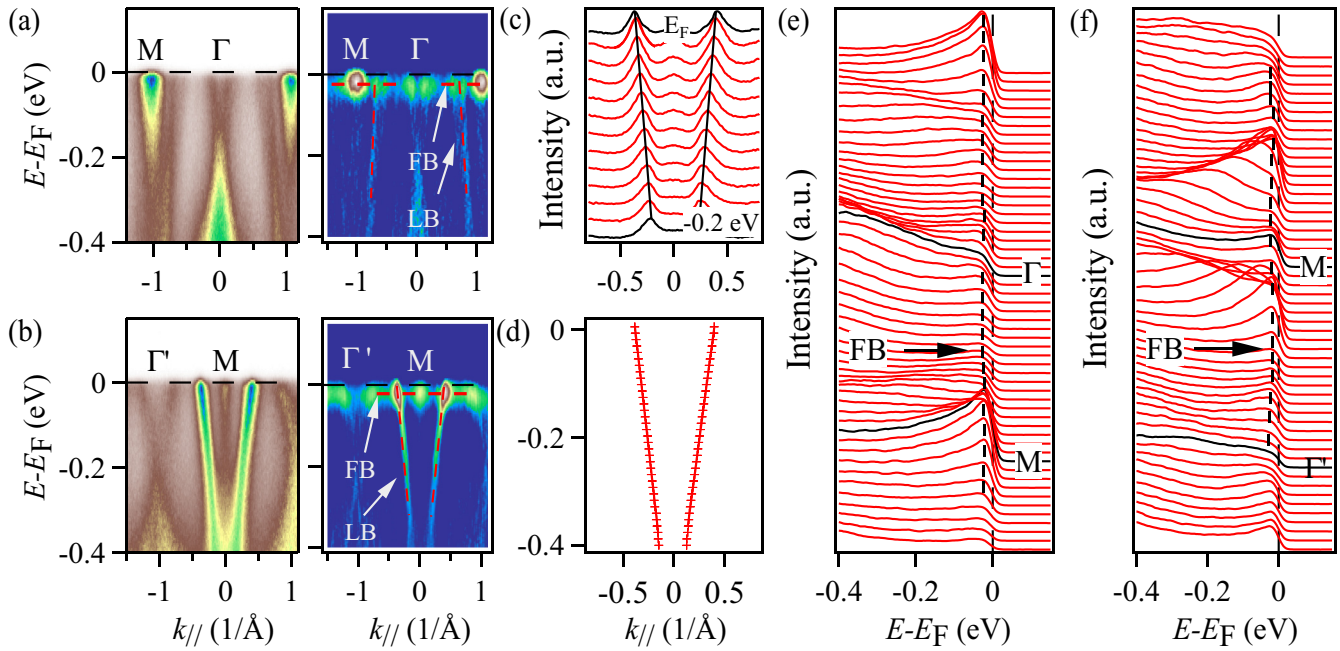

FIG. 3. (a) and (b) Intensity plots and corresponding second derivative plots along the Γ-M and Γ′-M (perpendicular to Γ-M) directions, respectively. Flat bands (FB) and linear bands (LB) are indicated by the red dashed lines on the corresponding second derivative plots. (c) MDCs of (b) show linear bands. (d) Linear bands abstracted from the fitted MDCs. (e) EDCs of (a). (f) EDCs of (b). The black dashed lines are guides to flat bands.

distribution curves (MDCs) in Fig. 2(c). The second derivative plot of Fig. 2(a) shows a band with negligible k_z dispersion around the BZ center, corresponding to the κ band around $\bar{\Gamma}$. The κ band extending to the $\bar{M}$ point and forming the flat band is more clearly observed on the nonsymmetry planes from around 84 to 98 eV due to the matrix element effects, as the shadows indicated by the red frames in Fig. 2(a), though the calculation indicates the flat band sinks deeply on the Γ-M plane Fig. 5(a). The second derivative plot of Fig. 2(b) shows a band with a periodic modulation along the k_z direction around the BZ corner, corresponding to the γ/δ band. The k_z dispersion of the β band bottom is displayed by energy distribution curves (EDCs) along the A-M-A direction in Fig. 2(d). Because the Fermi-Dirac function cuts off ARPES spectra at E_F, one cannot see obvious k_z dispersion of the β band bottom.

The flat band (κ) and the linear band (γ/δ) around the M point can be observed both along the Γ-M and Γ′-M directions (perpendicular to Γ-M), as shown in Figs. 3(a) and 3(b). By fitting MDCs and then extracting the dispersions, we observe the perfect linear dispersions with a wide energy range of ∼200 meV [Figs. 3(c) and 3(d)], and we obtain that the Fermi velocity is about 1.54 ± 0.01 eV Å (∼2.33×10^5 m/s) with $k_F \sim 0.39 \pm 0.02$ Å^{-1}. The linear bands show linear scattering rates up to 100 meV below E_F at low temperatures (Fig. 4 in Ref. [28]), consistent with anomalous temperature-dependent resistivity. To see the flat bands, EDCs along the Γ-M and Γ′-M directions were displayed in Figs. 3(e) and 3(f), which show the flat bands near E_F run through the Γ-M (Γ′-M) lines and cross the linear bands near the M point.

As mentioned above, the shadows in FSs [Fig. 1(b)] and k_z map [Fig. 2(a)] indicate that the flat bands will be more clearly observed on those non-high-symmetry planes. Accordingly, we show intensity plots along the $\bar{\Gamma}$-$\bar{M}$ direction taken by various photon energies in Fig. 4(a). The red flame in the 88-eV panel is a representation for indicating flat bands in all panels. These primitive intensity plots clearly show the existence of flat bands along $\bar{\Gamma}$-$\bar{M}$. EDCs of the intensity plot taken with 88-eV photons in Fig. 4(b) show the flat band with the marked peaks located about -0.03 eV below E_F. To remove the effect of the Fermi-Dirac function, the EDCs were symmetrized. Here, we chose and show the EDCs at the middle of the $\bar{\Gamma}$ and $\bar{M}$ points (k_{mid}) as a representative in Fig. 4(c). Only occupied parts of the symmetrized EDCs are displayed to avoid the misleading gaps and peaks above E_F induced by symmetrization. When the effect of the Fermi-Dirac function was removed, the peak positions of symmetrized EDCs would just be located at E_F. Due to the k_z broadening effect in ARPES spectra and the cutoff of the broad feature at E_F, within experimental resolutions, here we do not observe clear k_z dispersion of the flat band suggested by the calculation. It is similar to flat band in $Sr(Co_{0.9}Ni_{0.1})_2As_2$ [the red curves in Fig. 4(c)] [25], which has a smaller lattice constants ($a =$ 3.94 Å and $c = 11.773$ Å for $SrCo_2As_2$ [29]) than that of $Ba(Fe_{1/3}Co_{1/3}Ni_{1/3})_2As_2$ ($a = 3.9920$ Å and $c = 12.6191$ Å [28]). Therefore, with the smaller BZ, the chemical potential of the latter should be shifted up a bit.

Figure 5(a) shows DFT calculated bands by using the lattice constants of $BaCo_2As_2$ (red solid lines) and $Ba(Fe_{1/3}Co_{1/3}Ni_{1/3})_2As_2$ (black dashed lines), respectively. The calculated bands of the two materials almost coincide in the vicinity of E_F and deviate from each other at high binding energies. Thus, in a reasonable range of lattice constants, the flat band near E_F does not move. With the same number of average $3d$ electrons, the band structure is almost the same between $BaCo_2As_2$ and $Ba(Fe_{1/3}Co_{1/3}Ni_{1/3})_2As_2$, but there is a clear difference in the observed physical properties between

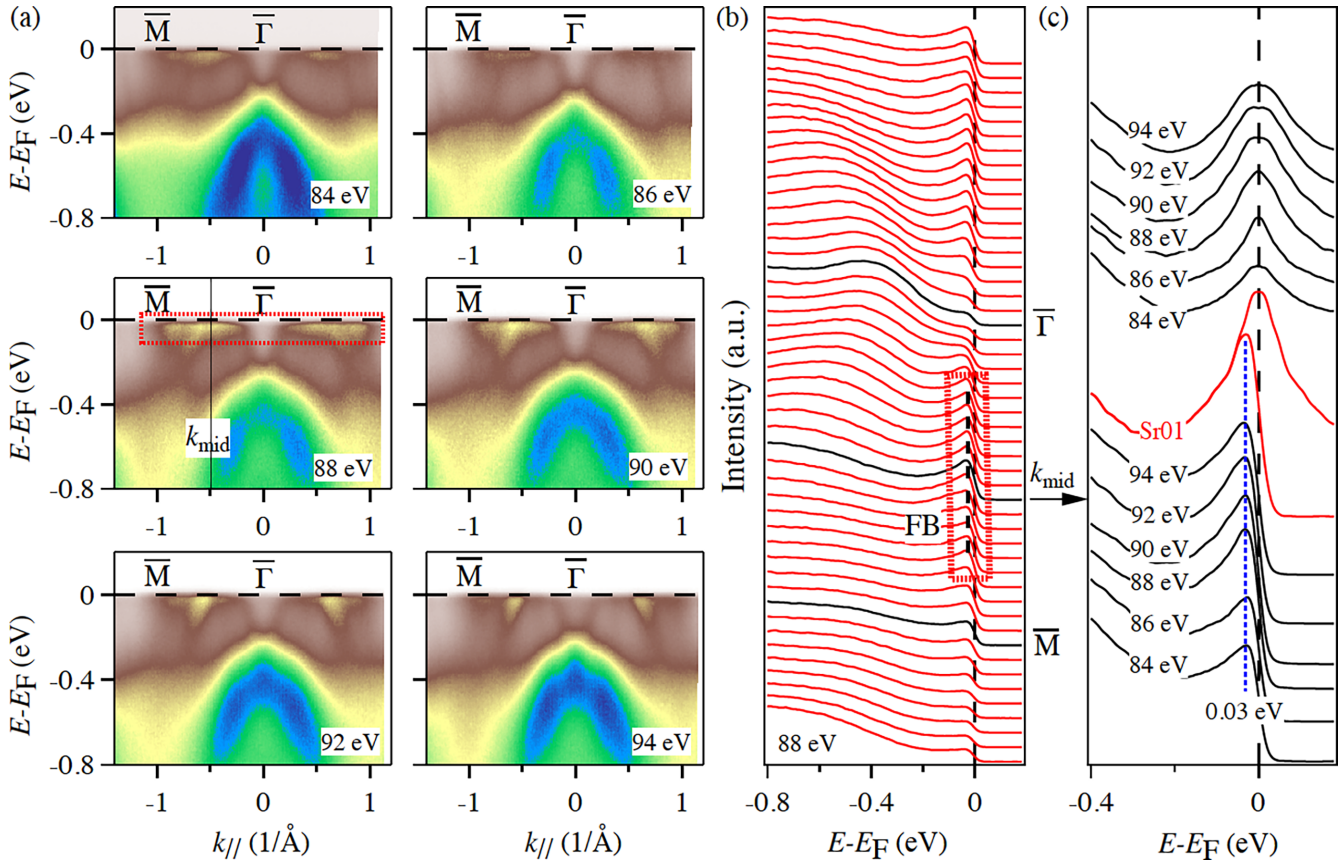

FIG. 4. (a) Intensity plots along the $\bar{\Gamma} - \bar{M}$ direction taken by photon energies of 84, 86, 88, 90, 92, and 94 eV, respectively, as noted in the individual panels. The red frame in one panel of 88 eV, as a representative, indicates the flat bands along $\bar{\Gamma} - \bar{M}$ in all panels and the k_{mid} is in the middle of $\bar{\Gamma} - \bar{M}$. (b) EDCs of the intensity plot taken with 88-eV photons in (a). The red frame indicates the flat band along $\Gamma - M$. (c) Black curves are the EDCs and symmetrized EDCs at k_{mid}. The red curves are the corresponding EDC and symmetrized EDC of $Sr(Co_{0.9}Ni_{0.1})_2As_2$ [25]. Symmetrization allows us to approximately remove the effect of the Fermi-Dirac function at k_F.

them [24,28]. The former with coexisting ferromagnetic and antiferromagnetic spin fluctuations is in proximity to a magnetic instability. Thus, different ground states and magnetic ordering types may be achieved by tuning the electronic structure. Our previous works have demonstrated that the flat band is responsible for the magnetic instability in $SrCo_2As_2$ [24] and has a close connection with the helical magnetic order in $Sr(Co_{0.9}Ni_{0.1})_2As_2$ [25]. The latter could be driven by quantum fluctuations and the system is likely in the vicinity of a quantum critical point [26,27], which provides experimental evidence of metallic quantum criticality enabled by flat bands as a theoretical prediction. As mentioned above, considering

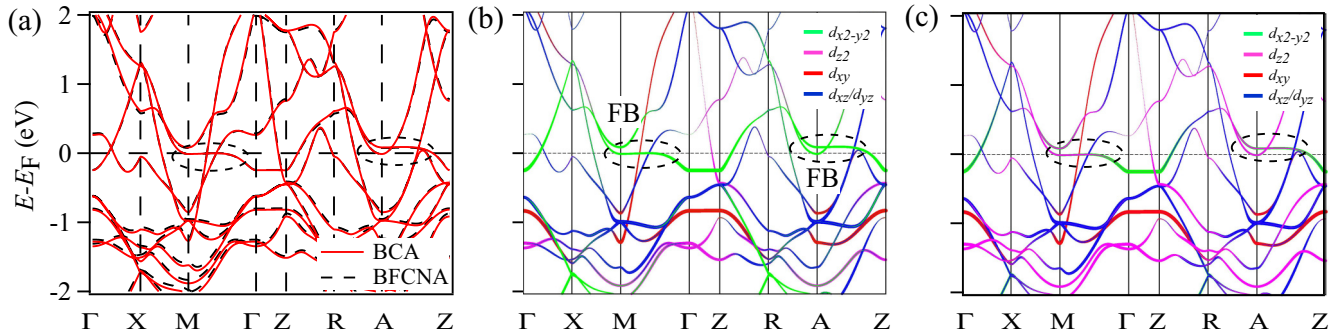

FIG. 5. (a) DFT calculation with spin-orbit coupling (SOC) along high-symmetry directions. Flat bands are indicated by the black ellipses. The experimental crystal structures (space group I4/mmm, No. 139) of $BaCo_2As_2$ (red solid lines) with lattice constants $a = 3.9537$ Å, $c = 12.6524$ Å, and $z_{As} = 1.278$ Å [34] and $Ba(Fe_{1/3}Co_{1/3}Ni_{1/3})_2As_2$ (black dashed lines) with lattice constants $a = 3.9920$ Å, $c = 12.6191$ Å, and $z_{As} = 1.282$ Å [28] were used in the calculations. (b and c) DFT calculation with SOC and 3d orbital projections along high-symmetry directions. d_{x2-y2} (green) orbital is mainly shown in (e), and d_{z2} (magenta) orbital is mainly shown in (f).

the differences in crystal lattice constants, the energy position of the flat band in $Ba(Fe_{1/3}Co_{1/3}Ni_{1/3})_2As_2$ is closer to that in $Sr(Co_{0.9}Ni_{0.1})_2As_2$ [Fig. 4(c)]. It may suggest that the existence of quantum criticality induced by the flat band in the $Ba(Fe_{1/3}Co_{1/3}Ni_{1/3})_2As_2$ is not purely coincidental. As confirmed by extensive studies in iron pnictides [28], the substitutions can modify the electronic structure subtly, but significantly enough to tune in and out of different ground states and correlation types. $Ba(Fe_{1/3}Co_{1/3}Ni_{1/3})_2As_2$ with the specific 1/3 equal ratios of Fe:Co:Ni can stabilize a unique quantum critical ground state. Thus, the scale invariance can be observed in substitutional alloying as in medium entropy alloys.

To study their orbital characters, we performed DFT calculations with orbital projections as shown in Figs. 5(b) and 5(c). The flat band is mainly dominated by d_{x2-y2} (green) orbitals and relatively less d_{z2} (magenta) orbitals. The linear band with d_{xy} orbital character (red) crosses the flat band at E_F, forming a collapsing point of lightweight quasi-electrons, as a black hole in a crystal universe. The DFT calculated bands need to be compressed by a factor of $\sim$1.4 to match the experimental results. While Hubbard $U = 5.0$ eV and Hund's rule coupling $J = 0.8$ eV are used in the previous calculation on ACo_2As_2 by fully charged self-consistent density functional theory plus dynamical mean-field theory (DFT+DMFT) [29], the mass enhancement obtained from the quasiparticle self-energy shows that the e_g orbitals, especially d_{x2-y2}, are more enhanced and correlated than the t_{2g} orbitals, indicating the orbital-selective physics is promoted by Hund's coupling.

IV. CONCLUSION

We have unambiguously demonstrated the existence of flat band and linear band with their orbital characters in the non-superconducting $Ba(Fe_{1/3}Co_{1/3}Ni_{1/3})_2As_2$, which is a good platform to study anomalous temperature-dependent quantum critical phenomena. The flat band just at E_F is responsible for quantum critical fluctuations, and the linear band with anomalous scattering rate exhibits non-Fermi-liquid behaviors. Our findings could stimulate studies of $3d$-electron flat band and linear band, and shed light on the exploitation of emergent physics.

ACKNOWLEDGMENTS

We acknowledge beamtime at a 1^3-ARPES end-station at BESSY. This work was supported by the National Key R&D Program of China (Grant No. 2022YFB3608000), the National Natural Science Foundation of China (NSFC, Grants No. 12222413 and No. 12074041), and the Natural Science Foundation of Shanghai (Grants No. 23ZR1482200 and No. 22ZR1473300). The calculations used high-performance computing clusters of Beijing Normal University in Zhuhai. Research at the University of Maryland was supported by the Gordon and Betty Moore Foundation's EPiQS Initiative through Grant No. GBMF9071, the U.S. National Science Foundation Grant No. DMR2303090, and the Maryland Quantum Materials Center.

[1] H. Tasaki, Prog. Theor. Phys. **99**, 489 (1998).
[2] Y. Cao, V. Fatemi, A. Demir, S. Fang, S. L. Tomarken, J. Y. Luo, J. D. Sanchez-Yamagishi, K. Watanabe, T. Taniguchi, E. Kaxiras, R. C. Ashoori, and P. Jarillo-Herrero, Nature (London) **556**, 80 (2018).
[3] E. Tang, J.-W. Mei, and X.-G. Wen, Phys. Rev. Lett. **106**, 236802 (2011).
[4] K. Sun, Z. Gu, H. Katsura, and S. D. Sarma, Phys. Rev. Lett. **106**, 236803 (2011).
[5] T. Neupert, L. Santos, C. Chamon, and C. Mudry, Phys. Rev. Lett. **106**, 236804 (2011).
[6] Y. Cao, V. Fatemi, S. Fang, K. Watanabe, T. Taniguchi, E. Kaxiras, and P. Jarillo-Herrero, Nature (London) **556**, 43 (2018).
[7] G. R. Stewart, Rev. Mod. Phys. **56**, 755 (1984).
[8] Z. Lin, J.-H. Choi, Q. Zhang, W. Qin, S. Yi, P. Wang, L. Li, Y. Wang, H. Zhang, Z. Sun, L. Wei, S. Zhang, T. Guo, Q. Lu, J.-H. Cho, C. Zeng, and Z. Zhang, Phys. Rev. Lett. **121**, 096401 (2018).
[9] J.-X. Yin, S. S. Zhang, H. Li, K. Jiang, G. Chang, B. Zhang, B. Lian, C. Xiang, I. Belopolski, H. Zheng, T. A. Cochran, S.-Y. Xu, G. Bian, K. Liu, T.-R. Chang, H. Lin, Z.-Y. Lu, Z. Wang, S. Jia, W. Wang *et al.*, Nature (London) **562**, 91 (2018).
[10] Y. Zhang, H. Lu, X. Zhu, S. Tan, W. Feng, Q. Liu, W. Zhang, Q. Chen, Y. Liu, X. Luo, D. Xie, L. Luo, Z. Zhang, and X. Lai, Sci. Adv. **4**, eaa06791 (2018).
[11] J.-X. Yin, S. S. Zhang, G. Chang, Q. Wang, S. S. Tsirkin, Z. Guguchia, B. Lian, H. Zhou, K. Jiang, I. Belopolski, N. Shumiya, D. Multer, M. Litskevich, T. A. Cochran, H. Lin, Z. Wang, T. Neupert, S. Jia, H. Lei, and M. Z. Hasan, Nat. Phys. **15**, 443 (2019).
[12] T. Y. Yang, Q. Wan, J. P. Song, Z. Du, J. Tang, Z. W. Wang, N. C. Plumb, M. Radovic, G. W. Wang, G. Y. Wang, Z. Sun, J.-X. Yin, Z. H. Chen, Y. B. Huang, R. Yu, M. Shi, Y. M. Xiong, and N. Xu, Quantum Front. **1**, 14 (2022).
[13] Z. Lin, C. Wang, P. Wang, S. Yi, L. Li, Q. Zhang, Y. Wang, Z. Wang, H. Huang, Y. Sun, Y. Huang, D. Shen, D. Feng, Z. Sun, J.-H. Cho, C. Zeng, and Z. Zhang, Phys. Rev. B **102**, 155103 (2020).
[14] M. Kang, L. Ye, S. Fang, J.-S. You, A. Levitan, M. Han, J. I. Facio, C. Jozwiak, A. Bostwick, E. Rotenberg, M. K. Chan, R. D. McDonald, D. Graf, K. Kaznatcheev, E. Vescovo, D. C. Bell, E. Kaxiras, J. van den Brink, M. Richter, M. P. Ghimire *et al.*, Nat. Mater. **19**, 163 (2020).
[15] Z. Liu, M. Li, Q. Wang, G. Wang, C. Wen, K. Jiang, X. Lu, S. Yan, Y. Huang, D. Shen, J.-X. Yin, Z. Wang, Z. Yin, H. Lei, and S. Wang, Nat. Commun. **11**, 4002 (2020).
[16] M. Kang, S. Fang, L. Ye, H. C. Po, J. Denlinger, C. Jozwiak, A. Bostwick, E. Rotenberg, E. Kaxiras, J. G. Checkelsky, and R. Comin, Nat. Commun. **11**, 4004 (2020).
[17] P. Dai, Rev. Mod. Phys. **87**, 855 (2015).
[18] D. J. Scalapino, Rev. Mod. Phys. **84**, 1383 (2012).
[19] L. de' Medici, G. Giovannetti, and M. Capone, Phys. Rev. Lett. **112**, 177001 (2014).
[20] Z.-H. Liu, A. N. Yaresko, Y. Li, D. V. Evtushinsky, P.-C. Dai, and S. V. Borisenko, Appl. Phys. Lett. **112**, 232602 (2018).

[21] Z. H. Liu, Y. G. Zhao, Y. Li, L. L. Jia, Y. P. Cai, S. Zhou, T. L. Xia, B. Büchner, S. V. Borisenko, and S. C. Wang, J. Phys.: Condens. Matter **27**, 295501 (2015).
[22] N. Xu, P. Richard, A. van Roekeghem, P. Zhang, H. Miao, W.-L. Zhang, T. Qian, M. Ferrero, A. S. Sefat, S. Biermann, and H. Ding, Phys. Rev. X **3**, 011006 (2013).
[23] R. S. Dhaka, Y. Lee, V. K. Anand, D. C. Johnston, B. N. Harmon, and A. Kaminski, Phys. Rev. B **87**, 214516 (2013).
[24] Y. Li, Z. Yin, Z. Liu, W. Wang, Z. Xu, Y. Song, L. Tian, Y. Huang, D. Shen, D. L. Abernathy, J. L. Niedziela, R. A. Ewings, T. G. Perring, D. M. Pajerowski, M. Matsuda, P. Bourges, E. Mechthild, Y. Su, and P. Dai, Phys. Rev. Lett. **122**, 117204 (2019).
[25] Y. Li, Z. Liu, Z. Xu, Y. Song, Y. Huang, D. Shen, N. Ma, A. Li, S. Chi, M. Frontzek, H. Cao, Q. Huang, W. Wang, Y. Xie, R. Zhang, Y. Rong, W. A. Shelton, D. P. Young, J. F. DiTusa, and P. Dai, Phys. Rev. B **100**, 094446 (2019).
[26] N. S. Sangeetha, L.-L. Wang, A. V. Smirnov, V. Smetana, A.-V. Mudring, D. D. Johnson, M. A. Tanatar, R. Prozorov, and D. C. Johnston, Phys. Rev. B **100**, 094447 (2019).
[27] J. M. Wilde, A. Kreyssig, D. Vaknin, N. S. Sangeetha, B. Li, W. Tian, P. P. Orth, D. C. Johnston, B. G. Ueland, and R. J. McQueeney, Phys. Rev. B **100**, 161113(R) (2019).
[28] Y. Nakajima, T. Metz, C. Eckberg, K. Kirshenbaum, A. Hughes, R. Wang, L. Wang, S. R. Saha, I. L. Liu, N. P. Butch, D. Campbell, Y. S. Eo, D. Graf, Z. Liu, S. V. Borisenko, P. Y. Zavalij, and J. Paglione, Commun. Phys. **3**, 181 (2020).
[29] H. Mao and Z. Yin, Phys. Rev. B **98**, 115128 (2018).
[30] Z. P. Yin, K. Haule, and G. Kotliar, Nat. Phys. **7**, 294 (2011).
[31] Z.-H. Liu, P. Richard, N. Xu, G. Xu, Y. Li, X.-C. Fang, L.-L. Jia, G.-F. Chen, D.-M. Wang, J.-B. He, T. Qian, J.-P. Hu, H. Ding, and S.-C. Wang, Phys. Rev. Lett. **109**, 037003 (2012).
[32] P. Blaha, K. Schwarz, G. Madsen, D. Kvasnicka, and J. Luitz, *WIEN2k, An Augmented Plane Wave + Local Orbitals Program for Calculating Crystal Properties* (Karlheinz Schwarz, Techn. Universität Wien, Austria, 2001).
[33] J. P. Perdew, K. Burke, and M. Ernzerhof, Phys. Rev. Lett. **77**, 3865 (1996).
[34] A. S. Sefat, D. J. Singh, R. Jin, M. A. McGuire, B. C. Sales, and D. Mandrus, Phys. Rev. B **79**, 024512 (2009).